Modified Solar Cell BRDF

Madilynn E. Compean
Air Force Institute of Technology, 2950 Hobson Way, Wright-Patterson AFB, OH 45433
Todd V. Small
Air Force Institute of Technology, 2950 Hobson Way, Wright-Patterson AFB, OH 45433

ABSTRACT

Light curve analysis is an alternative method used to investigate satellite activity, particularly in situations where high-resolution imagery from ground-based optical systems is impossible, such as geosynchronous satellite observations. Glinting features found in reflection patterns from satellites provide important distinguishing information, but large errors have been documented when trying to model such features. The bidirectional reflectance distribution function (BRDF) describes the spatial distribution of a material's reflectance as the ratio of the incident irradiance to scattered radiance, and BRDFs play an essential role in simulating light curves and interpreting light curve observations. BRDFs are a function of five variables, which includes two angles to describe the incident ray direction, two angles to describe the scattered ray direction, and wavelength. Due to their dependence on angles, BRDFs can be highly dependent on illumination and observation geometry. A common category of BRDF - microfacet models - uses a combination of geometrical optics with a stochastic description of surface roughness. Microfacet models typically make simplifying assumptions which trade simulation accuracy for improved computing speed in scene generation applications. Another class of BRDF - physical optics models - are typically more radiometrically accurate but have greater complexity and increased needs for computing power. Due to the geometrical optics basis of microfacet models, they fail to account for wave optics effects such as diffraction. Physical optics models easily account for wave effects, but there is an underlying assumption that the surface is completely characterized.

In previous work, the microfacet formulation was abandoned for modeling solar cell BRDFs; instead, wave optics techniques were used to account for distinct solar cell diffraction features, capitalizing on improved accuracy while retaining closed-form solutions which avoided significant increases in computational cost. This current work specifically continues the experimental validation of the physical optics model. In particular, it presents in-plane, off-specular BRDF measurements containing features for which even the current physical optics model does not account. By reconciling the model's assumptions with the experimental results, this work shows that an updated shadowing term should be considered. Additional simulations are then conducted which explore the impact of various parameters within the model. The results highlight potentially interesting and important features, which provide ideas for even further experimental validation.

In BRDF coordinates, the origin is located in the solar panel plane, and each location on the Earth is associated with a particular scatter direction relative to that origin. In certain geometries, the solar cell's diffraction pattern may scatter across the Earth's surface, so that peaks in brightness may be observed in situations where the typical law of reflection would be not satisfied for purely specular reflection. The diffraction pattern peaks which contribute to off-specular signals on the Earth's surface are not currently included in typical microfacet models, which usually assume simple, isotropic surfaces; the diffraction has only recently been taken into account with a physical optics model formulation. Ultimately, failing to account for conical, multi-slit and shadowing diffraction effects from a solar panel leaves open the possibility of mis-modeling and mis-interpreting such reflection within light curves.

1. INTRODUCTION

In these unprecedented times, maintaining strategic advantage in space continues to be a key element to the military's joint strategy. It is imperative to continually improve our ability to detect, identify and characterize space targets. According to the Joint Space Operations doctrine, "Situational awareness [Space Domain Awareness (SDA)] is fundamental to conducting space operations. SDA is the requisite foundational, current, and predictive knowledge and characterization of space objects and the OE (Operational Environment) upon which space operations depend—including

physical, virtual, information, and human dimensions—as well as all factors, activities, and events of all entities conducting, or preparing to conduct, space operations...SDA must incorporate understanding of the space capabilities and intent of those that pose a threat to our space operations and space capabilities " [1]. Continually improving SDA capabilities is necessary to maintain the nation's edge in space dominance. Operators want better predictive capabilities to fully capture a space object's capabilities, its potential uses, and normal versus abnormal patterns of behavior [12].

One technique to aid in SDA is light curve analysis, which can help with understanding satellite activities in low-resolution scenarios. Geosynchronous satellite observations provide an example of low-resolution scenarios in which satellites are too far away from ground-based telescopes to obtain resolved imagery. Instead, scientists collect unresolved light signals over time (light curves), and then use radiometry to try to understand or infer situations or characteristics that caused the light curve. In radiometric equations, the impact of the material surface of a satellite must be considered and is contained within the bidirectional reflectance distribution function (BRDF), often denoted f_r. Often, solar cells comprise relatively large surface areas on satellites, and moreover, solar cells often possess relatively complicated surface characteristics. It follows that improving solar cell modeling should directly improve overall satellite radiometric modeling, and thus light curve analysis. Recently, a novel and predictive solar cell model was formulated based solely on surface characteristics, and the diffraction behavior in the model was validated with measurements in the near-specular region for a particular solar cell sample [6]. In this paper, experimental results are extended to the off-specular scatter region at two different incident angles ($\theta_i = 15^\circ$ and $\theta_i = 40^\circ$) using a second solar cell sample. The results indicate that solar cell BRDFs need to consider shadowing effects, which were previously unmodeled, but whose impact can vary depending on the particular solar cell surface structure.

2. BACKGROUND

2.1 Light Curve Analysis and Error

Measuring and evaluating the brightness of satellites over extended time intervals is known as light curve analysis. This technique can be used by analysts to examine certain characteristics, for instance whether a satellite is actively controlled or tumbling. Furthermore it can be used to identify separate satellites that are within close proximity, particularly by understanding glinting patterns within the observation. The brightness of a satellite depends on its distance from the observation point, its material properties, and the geometry of its orbital location and attitude relative to the light sources and observer [3]

In light curve analysis, new observations can be compared to both previous observations and radiometric simulations. Patterns based on previous observations can be used as baselines for first-order anomaly detection, in which changes in observation patterns indicate possible changes in satellite characteristics. Radiometric models that account for various aspects of optical energy transport within a scenario, including material reflection properties, can provide additional information about how certain satellite activities can map to changes in light curve observations. However, documented evidence suggests that radiometric simulations can suffer from large errors during glinting phenomena [2, 8]. In particular, solar cells are often modeled using isotropic microfacet BRDFs, despite possessing complex and clearly anisotropic surface features; those features are capable of producing wavelength-dependent diffraction effects which have been observed experimentally [17]. Thus, improvements in solar cell BRDF models provide an avenue for potentially improving satellite radiometric simulations and light curve analysis in general.

2.2 Radiometry

Radiometry is the science of tracking the directional power flow of optical energy through a system [9]. Radiative transfer accounts for the propagation of electromagnetic radiation from source to sensor, and includes the radiation's interactions with objects, the atmosphere, and environmental conditions. Generally, radiometric software defines the geometry of the scene and tracks the path of radiation through that scene, which requires models of the location and emission properties of energy sources, the location and properties of scattering objects, and the location and properties of the detector. The path of light rays are traced from material to object to detector. Often, for simplicity, complex material surfaces will be modeled as diffuse (Lambertian) reflectors, which assume equal energy is reflected into all angles. However, the Lambertian assumption sacrifices the accuracy which can be captured with more nuanced directionally-dependent BRDFs. The rendering equation can be used to help simulate a scene under observation [11],

$$L_s(\hat{\omega}_s, \lambda) = L_e(\hat{\omega}_s, \lambda) + \int_\Omega f_r(\hat{\omega}_i, \hat{\omega}_s, \lambda) L_i(\hat{\omega}_i, \lambda) cos(\theta_i) d\hat{\omega}_i, \tag{1}$$

where L_s is the total spectral radiance directed outwards in the direction of a detector ($\hat{\omega}_s$); f_r is the BRDF of a scattering surface; L_i is the spectral radiance reaching a scattering surface from an incident direction ($\hat{\omega}_i$); and the integral is over the incident hemisphere Ω. Spectral radiance from emitting sources is denoted L_e; emitted radiance can be considerable in the mid-wave or long wave infrared, but when considering space objects at visible wavelengths, L_e can be ignored.

The incident and scatter directions $\hat{\omega}_i$ and $\hat{\omega}_s$ in Eq. 1 are unit vectors, and can be written using more typical spherical coordinates as

$$\hat{\omega}_i = \begin{pmatrix} 1 \\ \theta_i \\ \phi_i \end{pmatrix} \text{ and } \hat{\omega}_s = \begin{pmatrix} 1 \\ \theta_s \\ \phi_s \end{pmatrix}. \tag{2}$$

From [7], the signal received by a ground-based detector from a satellite in geostationary orbit is given by

$$\Phi_{sig} = f_r(\theta_i, \phi_i, \theta_s, \phi_s) L_{sun}(\lambda, \Delta\lambda) \Omega_{sun} A_{opt} \Omega_{tar}, \tag{3}$$

where L_{sun} is the radiance emitted by the sun, which can be described using the blackbody equation; Ω_{sun} is the solid angle subtended by the sun from the satellite; Ω_{tar} is the field of view subtended by the target from the detector, which in this case is the solar panel of the satellite [7]; and A_{opt} is the area of the detector's optical aperture. $\Delta\lambda$ is the detection bandwidth for the radiance of the sun when using a bandpass filter. At geostationary distances, the irradiance received by the detector from the satellite (Φ_{sig}) is roughly a constant scaled by the BRDF f_r. From this equation, then, we conclude that BRDF is a crucial term to understanding the expected signal from a satellite.

2.3 Bi-Directional Reflectance Distribution Functions

Processes such as transmission, reflection, and refraction are macroscopic expressions of microscopic scattering interactions. BRDFs describe the spatial distribution of macroscopic reflection from a material surface [13, 19]. Scattering from a rough surface is typically modeled using BRDFs. In practice, semi-empirical models approximate the BRDF of a material based on a few experimentally measured values and various estimated parameters within a mathematical representation. However, fully measuring BRDFs in a laboratory setting can be challenging, because measuring the amount of light reflected into many different scatter angles for multiple wavelengths and incident angles can be cumbersome and unrealistic. In addition, models based on empirical data tend to be very specific to certain materials, and lack true predictive power.

There are hundreds of existing mathematical models for BRDFs, ranging from simple to extremely complex, which capture reflection behavior with varying levels of accuracy. Two common categories of analytical BRDF models are microfacet models and physical optics models [20]. Microfacet models assume geometrical optics and use a stochastic distribution of perfectly reflecting microfacet orientations to describe a material's surface; these relatively simple formulations lose accuracy but increase computational speed in simulations and scene rendering [4, 5]. Geometrical optics treats light as rays rather than waves, approximating light and energy propagation with straight-line paths. It typically provides a good approximation when wavelengths are small compared to material structure dimensions. However, fundamentally, it does not account for wave-optics effects such as diffraction and interference, and therefore fails in situations where periodic structures cause constructive and destructive interference [10]. Physical optics models, which are based on fundamental electromagnetic theory, use first principles to describe how light interacts with surfaces. Such models have the ability to include wave effects such as diffraction and interference in order to achieve greater accuracy, but typically at the expense of slower computational speeds [20]. Furthermore, physical optics models still have to make simplifying assumptions about surfaces, since perfect surface characterization on the wavelength scale is usually impractical [19, 4].

3. PHYSICAL EQUIVALENCE BRDF

Recently, a new solar cell BRDF was published based on fundamental electromagnetic theory using the geometry shown in Fig. 1 [6]. In the development, $\bar{E}_i$ is the incident electromagnetic field arriving from (θ_i, ϕ_i), and the reflection is observed at (θ_s, ϕ_s). The solar cell's surface was composed of thin metal conducting wires spaced periodically atop the photovoltaic material, whose top layer was Indium Gallium Phosphide (InGaP). The resulting model accounts for

diffraction effects from both the metal wires and the InGaP segmentation, and can be written in the form of a BRDF as

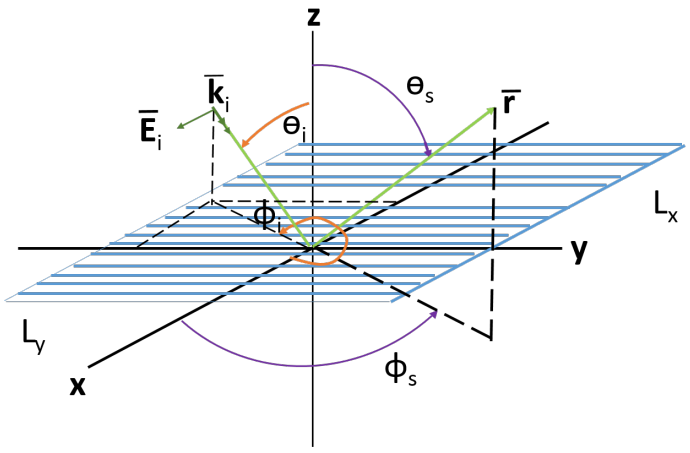

Fig. 1: 3D view of solar panel geometry used for general physical optics model development under monochromatic plane wave illumination. The geometry of the solar cell's orientation is fixed; however, the incident beam can rotate by changing θ_i and ϕ_i.

$$f_{sc} = \frac{1}{A_r}\left(\frac{\omega\mu}{4\pi\eta}\right)^2 \left[\left[\cos\theta_s\cos\theta_i\sin\left(\phi_s-\phi_i\right)\right]^2+\left[\cos\theta_i\cos\left(\phi_s-\phi_i\right)\right]^2\right]$$
$$L_y^2\,\mathrm{sinc}^2\left[k\frac{L_y}{2}\left(\sin\theta_s\sin\phi_s+\sin\theta_i\sin\phi_i\right)\right]\frac{\sin^2\left[Nk\frac{D}{2}\left(\sin\theta_s\cos\phi_s+\sin\theta_i\cos\phi_i\right)\right]}{\sin^2\left[k\frac{D}{2}\left(\sin\theta_s\cos\phi_s+\sin\theta_i\cos\phi_i\right)\right]}$$
$$\left\{d_I^2\left|1-r_{\perp I}\right|^2\mathrm{sinc}^2\left[k\frac{d_I}{2}\left(\sin\theta_s\cos\phi_s+\sin\theta_i\cos\phi_i\right)\right]+d_M^2\left|1-r_{\perp M}\right|^2\mathrm{sinc}^2\left[k\frac{d_M}{2}\left(\sin\theta_s\cos\phi_s+\sin\theta_i\cos\phi_i\right)\right]\right\}. \tag{4}$$

Details can be found in [6], but I and M are the numbers of illuminated InGaP and wire segments, respectively (assumed to be even), L_y is the illuminated size of the solar cell in the y direction, D is the center-to-center spacing between aluminum wires, d_M is the width of a wire, and d_I is the width of an InGaP segment between wires. Wavelength dependence is embedded within the frequency ω and wave number k of the incident beam. Material parameters such as index of refraction are embedded within the Fresnel amplitude coefficients $r_{\perp I}$ and $r_{\perp M}$ for the InGaP and metal wires, respectively. Finally, A_r is the area of the receiver.

This BRDF can predict the expected directional reflection from a solar cell based only on knowledge of its surface characteristics. A specific instance of this approach can be reduced to a Fourier transform of the surface structure when the diffraction pattern is either totally out-of-plane ($\phi_i = 90°$) or in-plane ($\phi_i = 180°$). Using the Fourier approach increases the ability to account for near- and far-field effects, and account for more than just plane-wave illumination.

4. MEASUREMENT TOOLS AND EXPERIMENTAL SETUP

The Complete Angle Scatter Instrument (CASI®) is a tool used to characterize the reflected and transmitted light from material samples. A CASI was used to measure the BRDF of a solar cell sample using a green HeNe laser as the source. The CASI's optics box was used to control the path and focus of the incident beam, and a connected graphical user interface (GUI) was used to mechanically maneuver goniometers to adjust both the incident angle on the sample

and the scatter angle location of the detector. In an augmented form, the CASI's detector becomes a charge-coupled device (CCD) array on the goniometer arm as shown in Fig. 2. In the CCD array configuration, each pixel serves as an individual detector and measures the reflected light in a unique scatter direction [18, 15, 14, 17]. Thus, at a single goniometer location, the CCD captures data across a range of both out-of-plane and in-plane scatter angles. The range of angles collected depends on the CCD's distance from the sample, and that distance is slightly adjustable (about 10-35 cm). However, the goniometer arm can also be slewed to different in-plane locations, allowing for a larger range of off-specular measurements to be captured.

For the experiments below, BRDF data was collected using a green HeNe laser (λ = 543 nm) with a solar cell whose metal wires were oriented so that the diffraction pattern was cast in the plane of incidence (in-plane). According to the azimuthal convention depicted in Fig. 1, from a simulation perspective $\phi_i = 180°$ in this scenario. The solar cell used in this work is a commercially available triple junction cell and is shown under illumination in Fig. 5. Data was collected at different exposure times and integrated to improve the dynamic range of the CCD. Ultimately, the goal of the following experiments was to extend the validation of the physical-optics-based solar cell BRDF model and inform further adjustments or considerations.

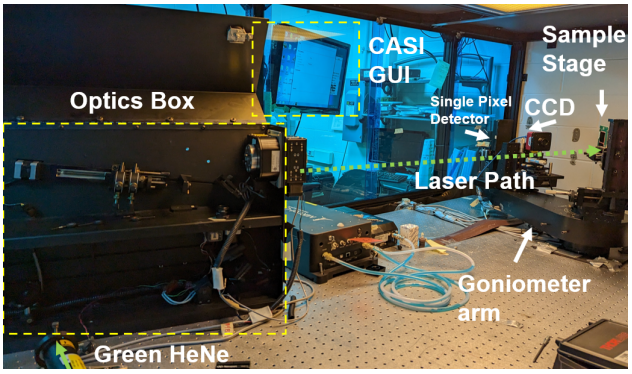

Fig. 2: Photograph of the CASI showing the solar cell in the sample holder on the right.

5. STITCHING EXPERIMENTS

One area of interest for the physical-optics-based model includes testing and validating the diffraction pattern farther away from the specular direction because a significant amount of energy can be contained in the diffraction wings. Experiments were performed to measure the energy in directions away from specular, and the measurements were compared to model simulations. Nominally, the CCD is placed about 32.5 cm from the material sample, and for a single measurement frame, the array captures a 3° range of scatter angles. In order to measure wider ranges of scatter angles, measurement frames need to be captured at different CASI goniometer locations, so that the frames can then be overlayed and stitched together spatially. Capturing data away from the specular peak and stitching frames together has the potential to introduce or magnify several sources of uncertainty. In particular, the detector arm's plane of rotation and the sample's plane of incidence may not be perfectly aligned, and any misalignment may be magnified as the CCD is slewed farther from specular. In addition, neutral density filters are required to attenuate the scattered signal just enough that none of the CCD's pixels are saturated within a particular frame. This means reducing the optical density (OD) of the filters for weaker signals in frames as the CCD moves away from specular, which leads to various OD levels in stitched frames. Unfortunately, OD is the largest documented source of measurement error in this system [16]. Fortunately though, the misaligment error is easily overcome, since the diffraction pattern lies somewhere within the CCD array even if it's not perfectly horizontal, and differences in OD levels can be overcome by slightly overlapping frames and scaling to match similar pixel readings.

Fig. 3 shows an example of stitched data when $\theta_i = 15°$ and Fig. 4 shows an example of stitched data when $\theta_i = 40°$. Multiple frames were used to collect data within $\pm 10°$ of the specular directions ($\theta_s = 15°$and $\theta_s = 40°$, respectively), and different colors represent the in-plane data slices through different frames. In both plots, the diffraction pattern does not appear as symmetric as one may expect. Data was then collected at both $\theta_i = -15°$ and $\theta_i = -40°$ which

reversed the forward scatter direction from the perspective of the CCD. The symmetry reversal in those results indicate that more work may be required to account for either a forward scattering effect, or the fact that the diffraction may be impacted by the shape of the illumination spot size.

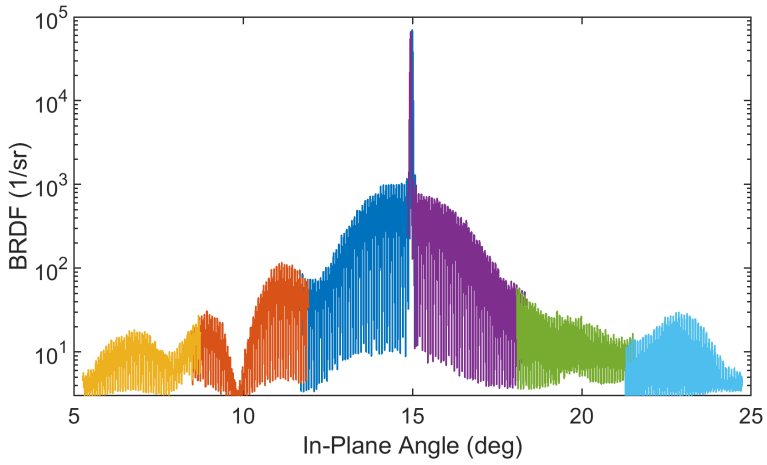

Fig. 3: Experimental data collected at $\theta_i = 15°$ on a second space qualified solar cell sample. The CCD was slewed off specular and stitched together to understand BRDF behavior across a larger angular range.

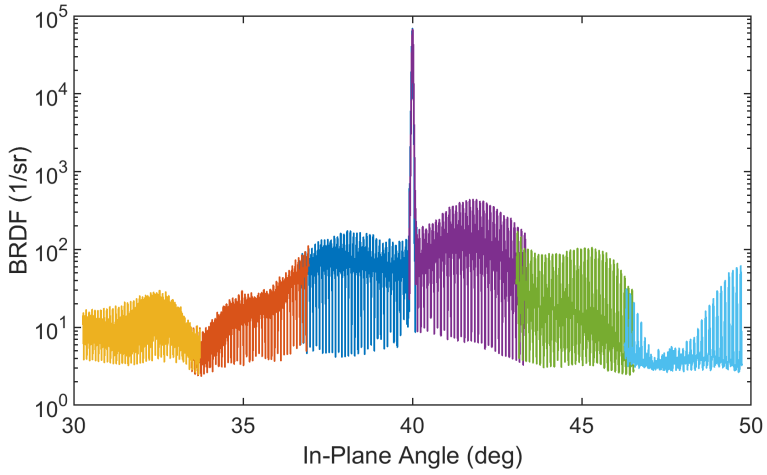

Fig. 4: Experimental data collected at $\theta_i = 40°$ on a second space qualified solar cell sample. The CCD was slewed off specular and stitched together to understand BRDF behavior across a larger angular range.

The right side of Fig. 5 shows a zoomed-in portion of Fig. 4 near the specular peak, while the left side of Fig. 5 provides an image to show what the illumination spot itself looks like on the solar cell. Roughly five metal grid lines are illuminated by the Gaussian beam, and subsidiary peaks in the data indicate corresponding multi-slit behavior. However, there is evidence of another interesting behavior that was not observed in previous validation work. In Figs. 4 and 5, starting from approximately $\theta_s = 38°$, the outer envelope decreases in magnitude as θ_s increases towards the specular peak at $\theta_s = 40°$, and then increases again as θ_s continues increasing towards $\theta_s = 42°$, showing a local minimum in the outer envelope in the specular direction. Normally, under the given illumination conditions, even when accounting for potential near-field effects in addition to far-field diffraction, model simulations are only able to produce an outer envelope maximum in the specular direction, so these experimental results indicate the potential presence of another phenomenon for consideration.

After investigating several aspects of the model, it was determined that the inclusion of a shadowing effect was able to recreate the outer envelope trough in the specular direction within the simulation. It is important to note that in the physical-optics-based formulation in [6], height differences between the metal grids and the underlying photovoltaic layer were ignored. However, particularly at steeper incident angles, it is possible that the raised metal grids block part of the InGaP segment from receiving illumination, as illustrated in Fig. 6. Thus, a shadowing compensation term was added to the model by keeping the periodicity and width of the metal wires the same, but scaling the illuminated width of the InGaP layer to decrease as θ_i increases.

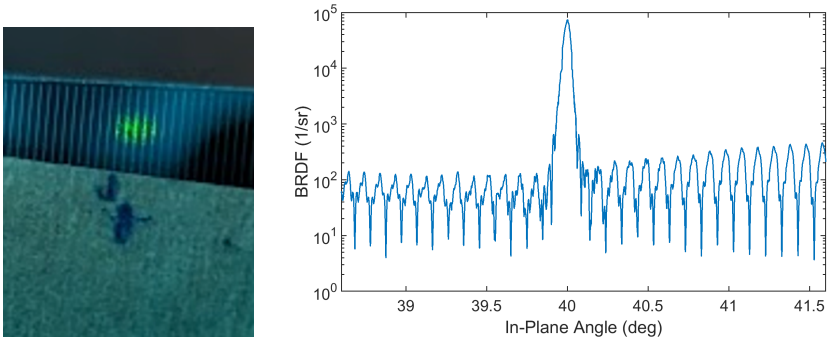

Fig. 5: (left) Image of the space-qualified solar cell with roughly 5 grid lines illuminated with a green HeNe laser. (right) Experimental BRDF data collected at $\theta_i = 40°$ on the space-qualified solar cell sample seen to the left. The BRDF shows multi-slit behavior, as expected, but also an unexpected local minimum in the outer envelope in the specular direction.

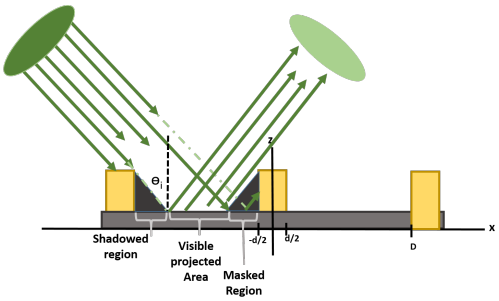

Fig. 6: An illustration of the effect of shadowing due to the structure of the surface of the solar cell.

Fig. 7 compares simulations of the solar cell's physical-optics-based BRDF model (using the Fourier formulation) both with and without accounting for shadowing (right and left, respectively). In both cases, the incident angle is set to $\theta_i = 40°$, and the dimensions and parameters associated with the solar cell surface structure are the same, but the shadowing term clearly impacts the outer envelope of the BRDF. Furthermore, the shadowing effect is not prevalent at shallower incident angles, such as $\theta_i = 15°$, although experiments should be conducted at more incident angles to confirm this behavior. It is also important to note that these results are valid assuming monochromatic illumination, which is required for highly resolved diffraction peaks and troughs. In reality, solar cells are illuminated by broadband sunlight, which tends to integrate the diffraction into a "streak," and so the shadowing effect on the outer envelope will likely not be noticeable in white light far-field observations and simulations. More experimental and simulated testing would be required to further understand the wavelength-integrated impact.

6. SIMULATION

The physical-optics-based solar cell BRDF model (especially with the Fourier formulation) has many parameters that can be adjusted to help simulations match experimental setups. In fact, simulated results can be used to intentionally

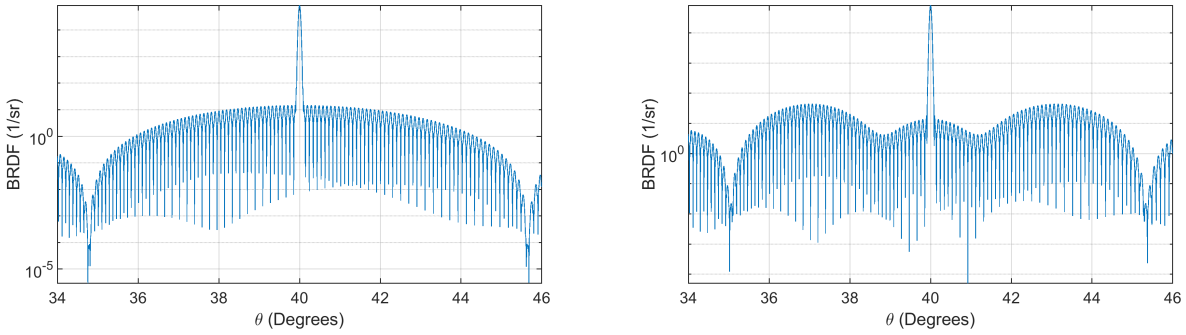

Fig. 7: Simulated results for a space-qualified solar cell before accounting for shadowing (left) and after accounting for shadowing (right), both at $\theta_i = 40°$, using the Fourier formulation of the physical-optics-based model.

explore the impact of parameter selection, which in turn can help inform interesting or important areas for future experimental testing and validation. For instance, one of the key updates included in the physical-optics-based solar cell BRDF is the ability to handle multi-slit features. Multi-slit features arise in the laboratory when using Gaussian laser sources to illuminate more grids with bigger beam sizes and different radius of curvature values. In particular, the radius of curvature can have dramatic impacts on the observed diffraction pattern.

6.1 Beam size and Radius of Curvature Variations

In the laboratory environment, where the CCD is less than a meter away from the sample, the diffraction pattern resulting from the InGaP segmentation (which accounts for most of the energy in the specular peak) is in the regime between the near-field and far-field, and is greatly impacted by the incident beam size and radius of curvature.

Fig. 8 shows simulated results when varying beam size, which in turn illuminates different numbers of metal grids on the solar cell surface. All simulations in this figure use $\lambda = 543$ nm and a radius of curvature $R_c = -100$ m, which is large enough to simulate plane wave illumination. The top two images are simulations with an observation distance of 32.5 cm, matching the nominal CCD distance from the solar cell in the experimental setup. On the top left is a zoomed-in version of the results on the top right. The top left shows the lower-frequency outer envelope pattern, while the top right shows the higher-frequency multi-slit behavior, in which subsidiary peaks occur in the same location, but are narrower. The bottom two images show simulation results with the same parameters, but at a simulated observation distance of 100 m. Ultimately, the outer envelope does not change with beam size, but the higher-frequency peaks do change and exhibit multi-slit behavior.

Fig. 9 shows simulated results at two different observation distances with various radius of curvature and beam size combinations based on realistic outputs from the CASI optics box, assuming a 543 nm Gaussian HeNe laser source and different CASI GUI focus parameters. The top plots correspond to an observation distance of 32.5 cm and the bottom plots correspond to an observation distance of 100 m. The zoomed-in plots on the left emphasize that beam size and radius of curvature can contribute to Fresnel-zone-like diffraction behavior when looking at the high-frequency peak patterns.

6.2 Wavelength Variations

Fig. 10 demonstrates simulation results using various wavelengths for two fixed beam sizes. The top plots show results with an illumination spot size of $w = 0.6$ mm, which corresponds to two-slit illumination conditions, and the bottom plots show results with a larger illumination spot size of $w = 2.2$ mm. The radius of curvature is fixed to $R_c = -0.8$ mm in all cases. The wavelength changes alter the spacing, shape, and location of both the high-frequency peaks and the lower-freqency outer envelope. In particular, the outer envelope modulates the overall pattern's magnitude. There are also indications that for given scenario parameters, shorter wavelengths exhibit more near-field-like complexity, which could support arguments to expand the wavelength diversity of experimental investigations.

6.3 Grid Width Variations

Fig. 11 shows simulated results in the far-field when the width of the metal grids was varied, but the width of the InGaP segments was held constant. As expected, adjustments to this parameter effected the outer envelope frequency.

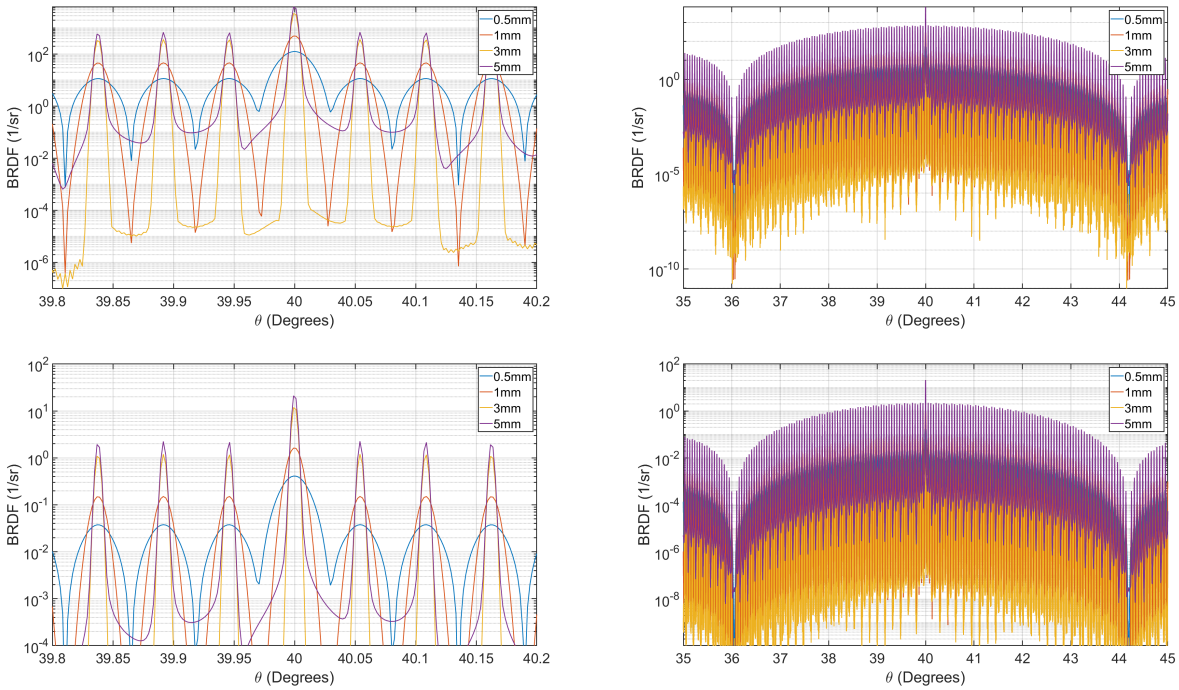

Fig. 8: (top) Simulated results with observation distance of 32.5 cm and radius of curvature $R_c = -100$ m illuminated by a 543 nm laser. (bottom) Same simulated parameters but with an observation distance of 100 m. Different colors indicate results with different beam sizes, and thus different numbers of metal grids illuminated in the solar cell surface.

Figure 12 shows simulated results when the width of the InGaP layer was varied, but the width of the metal grids was held constant. As expected, in this case, the outer envelop frequency remains unchanged, but the high-frequency peak spacing decreases as InGaP width increases.

In general, the simulations demonstrate that the detailed structure of the diffraction pattern reflected from a spacecraft solar cell can be highly dependent on the scenario parameters. Thus far, even when considering individual solar cell samples in a laboratory setting, experimental data does not match simulated magnitude. In order to perfect this physical-optics-based model, more work should be done to understand the diffraction pattern magnitude inconsistencies. Until then, simulation parameters must rely at least in part on experimental data, which challenges the goal of providing a model which successfully predicts both the relative shape and magnitudes of light scatter from solar cells.

7. CONCLUSION

Light curve analysis fundamentally uses radiometry to determine satellite activities from unresolved photometric observations. Within radiometric scene generators, BRDFs are used to describe the impact of a satellite's material surface characteristics on the reflected signal. Often, relatively large portions of satellite surface areas consist of solar panels. For accurate light curve analysis, solar cell BRDFs also need to be as accurate as possible. A recently published model [6] used fundamental electromagnetic principals to predict the reflection from a solar cell given its material structure. However, the work in this paper demonstrated a need to continue experimental validation to inform updates, such as shadowing effects. In particular, simulations from the new model showed a strong λ/D effect, indicating that knowing the surface structure of the solar cell is vitally important at optical frequencies.

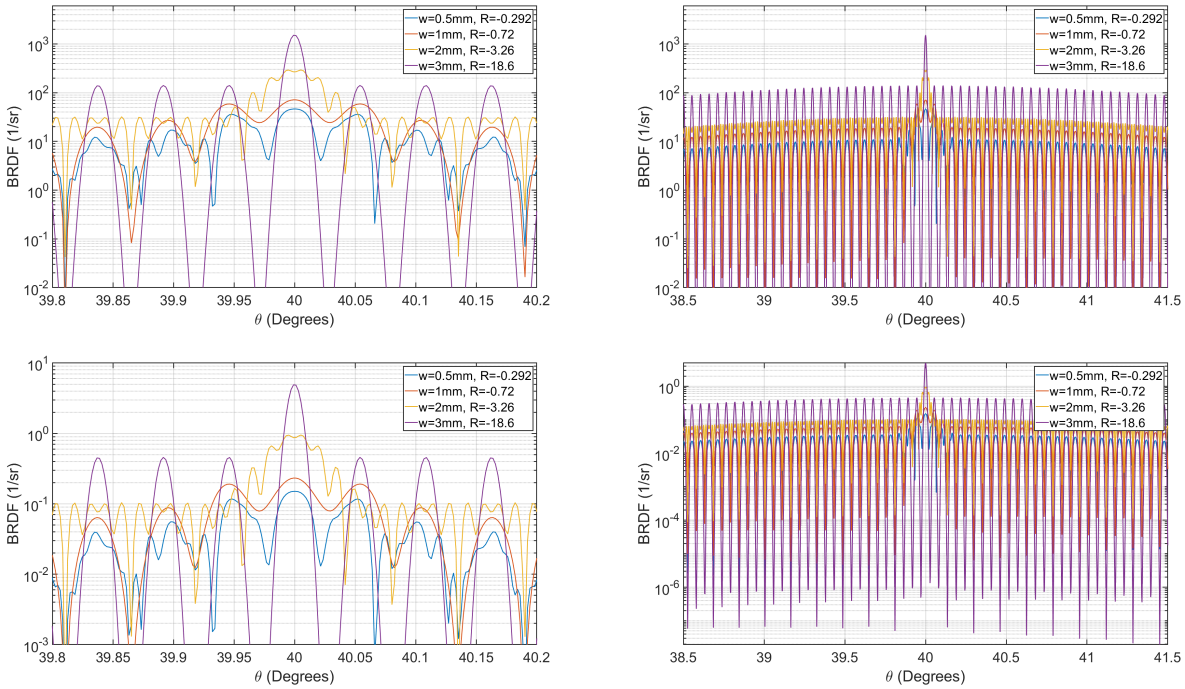

Fig. 9: Simulated results at two different observation distances but various beam size and radius of curvature combinations, assuming green HeNe Gaussian laser llumination. The top plots have an observation distance of 32.5 cm and the bottom plots have an observation distance of 100m.

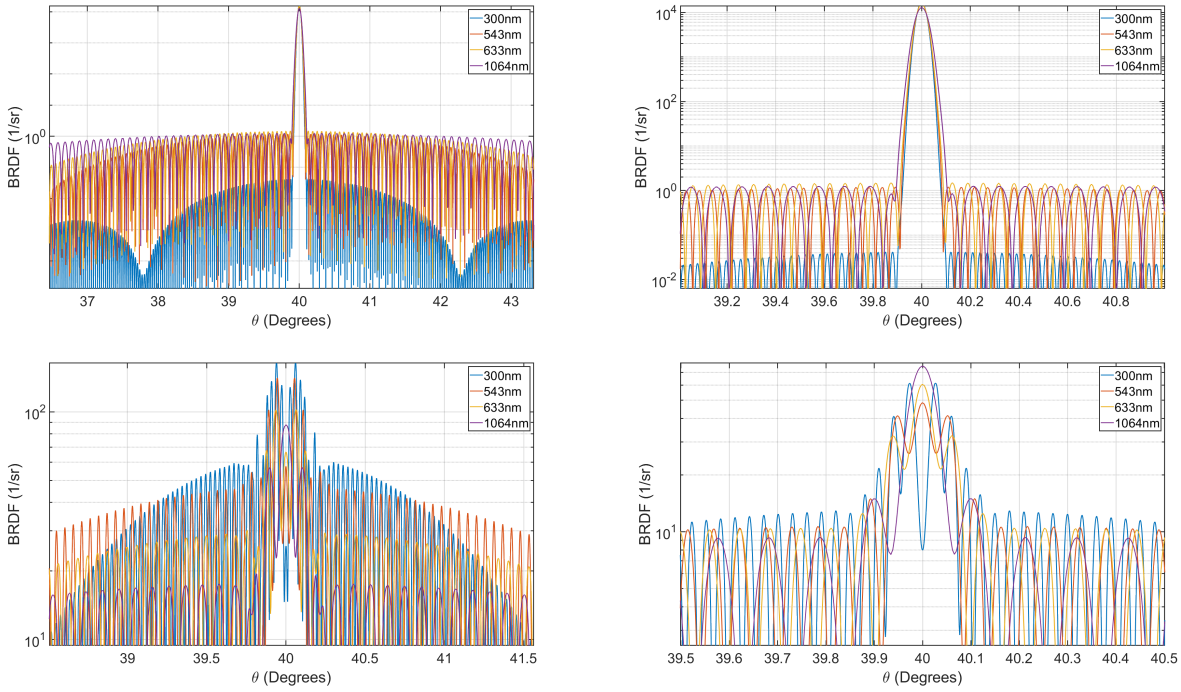

Fig. 10: Simulated results for various wavelengths at two beam sizes: 2-grid illumination (top) and multi-grid illumination (bottom). The wavelength changes cause noticable changes in the diffraction pattern spacing, location, and pattern, in both the high-frequency peaks and lower-frequency outer envelope.

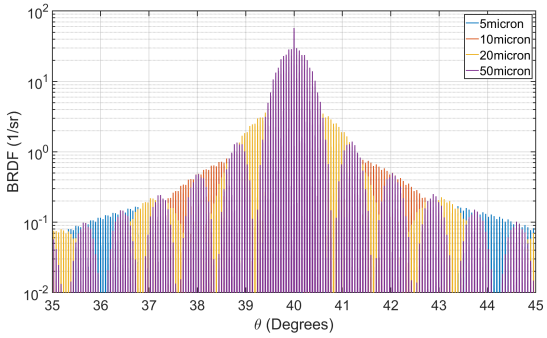

Fig. 11: Simulated results for various metal grid widths with InGaP segment width held constant. As expected, this variation affects the outer envelope frequency.

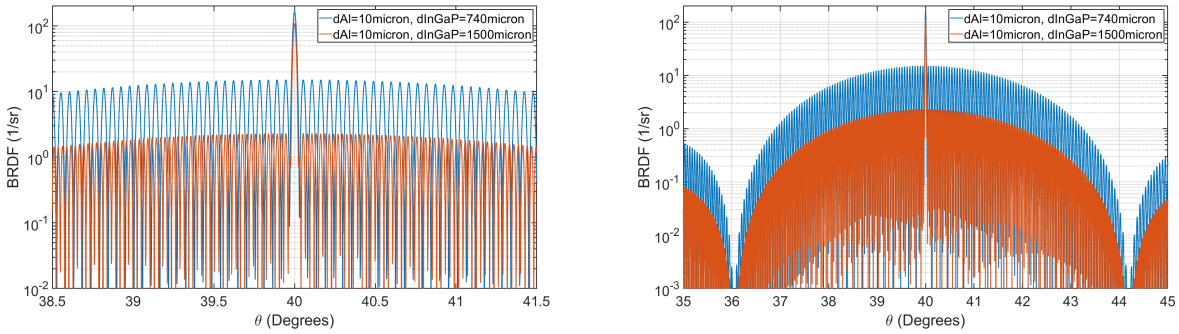

Fig. 12: Simulated results of expected changes due to varying the photovoltaic layer dimensions of the solar cell. The outer envelop stays the same, but as the width of the photovoltaic layer increase the number of peaks also increases, if the metal grid dimension is the same.

8. REFERENCES

[1] Joint Publication 3-14. Space operations. World Wide Web Page. Available at *https://www.jcs.mil/Portals/36/Documents/Doctrine/pubs/jp3_14ch1.pdf?ver=qmkgYPyKBvsIZyrnswSMCg*

[2] D. Bedard, M. Levesque, and B. Wallace. Measurement of the photometric and spectral BRDF of small Canadian satellites in a controlled environment. page E16, September 2011.

[3] Dennis Bonilla. Light curve analysis. World Wide Web Page. Available at *https://www.nasa.gov/content/asteroid-grand-challenge/characterize/light-curve-analysis*.

[4] S. Butler and M. Marciniak. "Robust Categorization of Microfacet BRDF Models to Enable Flexible Application-Specific BRDF Adaptation". *Society of Photographic Instrumentation Engineers, Publication 920506-1*, September 2014.

[5] S. Butler, S. Nauyoks, and M. Marciniak. "Robust Comparison of Microfacet BRDF Model Elements to Diffraction BRDF Model Element". *Society of Photographic Instrumentation Engineers, Publication 94720C-1*, August 2015.

[6] Madilynn Compean, Todd Small, Milo Hyde, and Michael Marciniak. Wave optics approach to solar cell brdf modeling with experimental results. *Optics Express*, 31(16):26289–26300, 2023.

[7] Madilynn E Compean, Todd V Small, and Michael A Marciniak. Microfacet based brdf solar cell model modification using experimental data. In *2023 IEEE Aerospace Conference*, pages 1–11. IEEE, 2023.

[8] Dao and Dentamaro. Resident space object characterization. Technical report, Air Force, 2016.

[9] M.T. Eismann and SPIE (Society). *Hyperspectral Remote Sensing*. Press Monographs. Society of Photo Optical, 2012.

[10] Hecht. *Optics, 5th Ed.* Pearson Education Inc., 2017.

[11] James T. Kajiya. The rendering equation. *SIGGRAPH Comput. Graph.*, 20(4):143–150, aug 1986.

[12] J. Lowery. "Measuring Light Curve Uncertainty for Surrogate Geostationary Satellite Models". Master's thesis, Air Force Institute of Technology, 2017.

[13] F. Nicodemus. Directional Reflectance and Emissivity of an Opaque Surface. *Applied Optics*, 4(7), 1965.

[14] J. Rifkin, K. A. Klicker, D. R. Bjork, D. R. Cheever, T. F. Schiff, J. C. Stover, F. M. Cady, D. J. Wilson, P. D. Chausse, and K. H. Kirchner. Design Review Of A Complete Angle Scatter Instrument. In Thomas C. Bristow and Alson E. Hatheway, editors, *Precision Instrument Design*, volume 1036, pages 116 – 124. International Society for Optics and Photonics, SPIE, 1989.

[15] Tod F. Schiff, John C. Stover, Daniel R. Cheever, and Donald R. Bjork. Maximum And Minimum Limitations Imposed On Bsdf Measurements. In Robert P. Breault, editor, *Stray Light and Contamination in Optical Systems*, volume 0967, pages 50 – 57. International Society for Optics and Photonics, SPIE, 1989.

[16] T. Small, S. Butler, and M. Marciniak. "Uncertainty Analysis for CCD-Augmented CASI BRDF Measurement System". *Optical Engineering*, 60(11), November 2021.

[17] Todd V. Small. *Improved Out-of-Plane BRDF Measurement and Modeling*. PhD thesis, Air Force Institute of Technology, 2023.

[18] Todd V. Small, Samuel D. Butler, and Michael A. Marciniak. Augmenting CASI® BRDF measurement device to measure out-of-plane scatter with CCD pixel array. In *Reflection, Scattering, and Diffraction from Surfaces VII*, volume 11485 of *Society of Photo-Optical Instrumentation Engineers (SPIE) Conference Series*, page 114850B, August 2020.

[19] Todd V. Small, Samuel D. Butler, and Michael A. Marciniak. Solar cell brdf measurement and modeling with out-of-plane data. *Optics Express35501*, 29(22), 2021.

[20] Rosana Montes Soldado and Carlos Ureña Almagro. An overview of brdf models. University of Granada, 2012.